https://doi.org/10.5194/acp-2022-851
Preprint. Discussion started: 20 February 2023

Atmospheric Chemistry and Physics
Discussions
Open Access

Occurrence frequency of Kelvin Helmholtz instability assessed by global high-resolution radiosonde and ERA5 reanalysis

Jia Shao[1]; Jian Zhang[2]*; Wuke Wang[3]; Shaodong Zhang[4]; Tao Yu[2]; Wenjun Dong[5,6]

[1] College of Informatics, Huazhong Agricultural University, Wuhan 430070, China
[2] Hubei Subsurface Multi-scale Imaging Key Laboratory, School of Geophysics and Geomatics, China University of Geosciences, Wuhan 430074, China
[3] School of environmental studies, China University of Geosciences, Wuhan 430074, China
[4] School of Electronic Information, Wuhan University, Wuhan 430072, China
[5] Center for Space and Atmospheric Research (CSAR), Embry-Riddle Aeronautical University, Daytona Beach, FL, USA
[6] Global Atmospheric Technologies and Sciences (GATS), Boulder, CO, USA

Correspondence to:
Dr. Jian Zhang (Email: zhangjian@cug.edu.cn)

https://doi.org/10.5194/acp-2022-851
Preprint. Discussion started: 20 February 2023

Atmospheric Chemistry and Physics Discussions

Abstract. Kelvin Helmholtz instability (KHI) is most likely to be the primary source for clear-air turbulence that is of importance in pollution transfer and diffusion and aircraft safety. It is exemplarily indicated by the critical value of Richardson (*Ri*) number, which is typically taken as 1/4. However, *Ri* is fairly sensitive to the vertical resolution of the dataset: a higher resolution systematically leads to a finer structure. The study aims to evaluate the performance of ERA5 reanalysis (137 model levels) in determining KHI spatial-temporal variabilities, by comparing it against a near-global high-resolution (10-m) radiosonde dataset during years 2017 to 2022, and to further highlight the global climatology and dynamical environment of KHIs. Overall, the occurrence frequency of *Ri*<1/4 in the free atmosphere is inevitably underestimated by the ERA5 reanalysis over all climate zones, compared to radiosonde, due largely to the severe underestimation in wind shears. Otherwise, the occurrence frequency of KHI indicated by *Ri*<1 in ERA5 is climatologically consistent with that from radiosondes in the free troposphere, especially over the midlatitude and subtropics in the Northern/Southern Hemisphere. Therefore, we infer that the threshold value of *Ri* should be approximated as 1, rather than 1/4, when using ERA5 for the KHI estimation. KHI occurrence frequencies revealed by both datasets exhibit significant seasonal cycles over polar, midlatitude, and subtropics regions, and they are consistently strong at heights of 10–15 km in the tropic region. In addition, the frequency at low-levels is positively correlated with the standard derivation of orography, and it is exceptionally strong over the Niño 3 region at heights of 6–13 km. Furthermore, the dynamical environment of KHI favors strong wind shears probably induced by the mean flows and the propagation of orographic or non-orographic gravity waves.

Key words: High-resolution radiosonde dataset; Kelvin Helmholtz instability; Threshold Richardson number; Gravity waves

https://doi.org/10.5194/acp-2022-851
Preprint. Discussion started: 20 February 2023

Atmospheric Chemistry and Physics Discussions

Introduction

Kelvin Helmholtz instability (KHI) is a common phenomenon in the atmospheric boundary layer and the free atmosphere (Muschinski and Wode, 1998), and its wavelengths and depths span a wide range of scales throughout the atmosphere, varying from few meters or less to 10s of km (Fritts et al., 2011). It contributes vertical mixing of heat, momentum, and constituents, and it acts to limit the maximum shears, just to name a few (Fritts et al., 2011). KHI along with gravity wave (GW) breaking are the most recognized instabilities in stably stratified flows (Fritts and Rastogi, 1985). In addition, GW breaking has been identified as important sources of instability (e.g., Fritts et al., 2020; Dong et al., 2020, 2021, 2022). KHI arises preferentially on strong shears due to medium-frequency and lower frequency GWs, tides, planetary waves (PWs), and mean flows (Baumgarten and Fritts, 2014). In addition, complex terrain may locally enhance wind shear, leading to KHI (Grasmick and Geerts, 2020). Large wind shear is common in regions where stability changes rapidly (e.g., near the top of the boundary layer) and the associated large gradient in jet stream (Grasmick and Geerts 2020), which may increase clear-air turbulence (Williams and Joshi, 2013). In turn, KHI can reduce wind shears and alter tracer gradients where turbulence and mixing are most intense (Fritts et al., 2022).

KHI influences depend on the spatial scales at which they lead to turbulence (Fritts et al., 2022). Turbulence is by far the most common cause of serious injuries to aircraft (Williams and Joshi, 2013). Convective instability, shear instability, KHI, and GW breaking are known to be the major source for turbulence (Sharman et al., 2012; Ko et al., 2019; 2022). Among others, KHI is one of the most common causes of turbulence throughout the atmosphere from Earth's surface to the lower thermosphere (Fritts et al., 2011; Sharman et al., 2012). KHI requires a sufficiently large Reynolds number and a Richardson (*Ri*) number sufficiently below 1/4 to enable KHI formation and subsequent secondary instability leading to turbulence (Fritts et al., 2022). *Ri* is not a good guide to instability character in general, and $Ri>1/4$ does not assure flow

https://doi.org/10.5194/acp-2022-851
Preprint. Discussion started: 20 February 2023

Atmospheric Chemistry and Physics Discussions

stability for superpositions of mean and GW motions. Despite these caveats, *Ri*<1/4 does provide a reasonable guide to expected local KHI structure in cases where clear KH billows arise (Fritts et al., 2014). Values of *Ri* close to zero favor strong instability, deep billows, and relatively intense turbulence, whereas values of *Ri* closer to 1/4 favor weak instability, shallow billows (Fritts et al., 2011). The threshold value of *Ri* can be potentially used an indicator of turbulence (for instance, Jaeger et al., 2007). Moreover, over half of turbulence exists below *Ri*<1 when the environment is beneficial for the development of turbulence (Zhang et al., 2022).

Turbulent mixing is of crucial importance to mass, energy, momentum transfer, the dispersion of pollutant, and stratosphere-troposphere exchange. However, it presents a challenge both in observation and numerical modeling (Sharman et al., 2012; Homeyer et al., 2014; Plougonven and Zhang, 2014). Due to the intermittent nature of turbulence it is generally not resolved in (global) numerical weather prediction models, even at nowadays common/states of the art horizontal resolutions of the order of tens of kilometers (Sandu et al., 2019).While in numerical models, turbulent dissipation rate, turbulent diffusivity and other parameters representing turbulent mixing efficiency are the most basic parameters, which need to be accurately parameterized to evaluate the impact of turbulent effect on matter and energy distribution (Gavrilov et al., 2005). For this reason, the indices of turbulence, such as large wind shear, small *Ri*, the negative squared Brunt-väisälä frequency, could be a great tool to characterize turbulence (Jaeger et al., 2007).

The *Ri* is estimated by the finite differences across thin layers and is quite sensitive to the vertical resolution of measurements (Haack et al., 2014). Thus, a proper estimation of *Ri* requires a high-resolution measurement of temperature and wind speed. The near-global distributed radiosonde site offers a unique opportunity to investigate the climatology of KHI occurrence frequency. The overview of KHI occurrence by using a near-global high-resolution (10-m) radiosonde data was presented in Zhang et al. (2022), and a close association between KHI occurrence frequency and turbulence fraction has been found. However, the global climatology characteristic of KHI remains most unclear, especially over oceans where the

https://doi.org/10.5194/acp-2022-851
Preprint. Discussion started: 20 February 2023

Atmospheric Chemistry and Physics Discussions

radiosonde network has a poor coverage.

By comparison, ERA5 global reanalysis can provide a seamless coverage of temperature and wind, and it is the last version of the European Centre for Medium-Range Weather Forecasts (ECMWF) model and has 137 model levels (Hersbach et al., 2020). It experiences a lot of improvements, including the statistically significant improvement in short-range forecasts by the Aeolus satellite (Rennie et al., 2021). Its predecessor, ERA-Intrim, was found in particular wind shear a factor of 2–3 lower simulated based on high-resolution radiosondes (Houchi et al., 2010). Moreover, results show that whatever the location and the geophysical conditions considered, biases between ERA-Interim and balloon wind measurements increase as a function of altitude (Duruisseau et al., 2017). Recent studies have suggested that the structure and variability of the trade winds in the lower troposphere are reasonably reproduced in the ERA5 reanalysis based on the EUREC4A field campaign (Savazzi et al., 2022). However, the similar comparison between ERA5 and high-resolution radiosonde across a near-global area has largely been undetermined. The proper estimation of wind shear and Brunt-Väisälä frequency is essential for the determination of *Ri*.

Thus, our objectives are to: (1) The performance of ERA5 (137 model levels) at different heights and climate zones in estimating wind shear and KHI occurrence frequency, comparing with a large high-resolution (10-m) radiosonde dataset spanning years from 2017 to 2022. (2) Based on the validation and comparison results, we pose a question: how to use ERA5 for KHI study? (3) The global climatology of KHI occurrence based on versatile measurements and products. (4) The dynamic environment (GWs and mean flow) of KHI. These works would be valuable for the understanding of the global distribution of KHI, and furthermore, turbulence fraction. To this end, this analysis is organized as follows. Section 2 shows the data and methods used. Section 3 represents the climatological variation of KHI and its comparison with radiosonde. Section 4 ends with a summary.

https://doi.org/10.5194/acp-2022-851
Preprint. Discussion started: 20 February 2023

2 Data and methods

2.1 High-resolution radiosonde dataset

As described in Guo et al. (2021) and Zhang et al. (2022), a high vertical resolution radiosonde (HVRRS) dataset gained from several organizations was adopted, spanning January 2017 to October 2022, in a total of 5.8 years. The organizations include the China Meteorological Administration (CMA), the U.S National Oceanic and Atmospheric Administration (NOAA), the Global Climate Observing System (GCOS) Reference Upper-Air Network (GRUAN), the Centre for Environmental Data Analysis of the United Kingdom (CEDA), University of Wyoming, Deutscher Wetterdienst, and ECMWF. In total, 115 million radiosonde profiles from 434 radiosonde stations released at regular synoptic times of 0000 UTC and 1200 UTC were collected to determine the value of *Ri*. These profiles were sampled at 0.5 Hz or 1 Hz, corresponding to a vertical resolution of approximately 10 m or 5 m. Thus, all the profiles were evenly interpreted to 10 m resolution in vertical by applying a cubic spline interpolation. In addition, the sounding with the burst height lower than 10 km above ground level (a.g.l) was directly discarded for further study. Meteorological variables, including temperature and wind speed, were prepared for the *Ri* estimation.

One of the shortage of radiosonde measurements is its inadequate concentration over the polar and ocean regions (Xia et al., 2021). The geographical distribution of total profile number of each radiosonde station is demonstrated in Figure S1 in Support Information. The released radiosoundings over Europe, the United States, and Australia have good geographical coverage and time duration. Over some islands of oceans (e.g., the Pacific Ocean) there are dozens of stations that can provide high-resolution measurement. Over the polar regions, there are around thirty stations.

2.2 ERA5 reanalysis and the collocation procedure

ERA5 is the latest version of ECMWF meteorological reanalysis, benefiting from

https://doi.org/10.5194/acp-2022-851
Preprint. Discussion started: 20 February 2023

a decade of developments in model physics, core dynamics, and data assimilation (Hersbach et al., 2020). The wind and temperature fields are modelled by the ERA5 reanalysis on a spatial resolution of 0.25° latitude/longitude and a temporal resolution of 1 hour. The reanalysis has 137 model levels, giving a vertical resolution of approximately 300 m in the middle and upper troposphere and 500 m in the lower stratosphere. The vertical resolution of ERA5 is illustrated in Figure S2. Compared to ERA5 reanalysis, the HVRRS is hard to provide global seamless observations. Thus, the collocation procedure between reanalysis and HVRRS goes as follows: (1) the matched grid of ERA5 reanalysis is the nearest neighbor of radiosonde station; (2) the regular synoptic start time of radiosonde and reanalysis needs to keep exact the same; (3) the pressure coordinate of reanalysis is converted into geometric altitude to match with HVRRS. In addition, the standard deviations of orography (SDOR) and near-surface wind speed at 10-m in ERA5 reanalysis are extracted.

The relative error between HVRRS-based and ERA5-based quantities is estimated by the ratio of deviations between HVRRS and ERA5 derived quantities to the HVRRS one.

2.3 The occurrence frequency of KHI and its uncertainty

The burst of KHI is characterized by the occurrence of the *Ri* under a critical value which is frequently taken as 1/4, and *Ri* is formulated as:

$$\mathrm{Ri} = \bar{N}^2/\bar{S}^2 \qquad (1)$$

where N is the Brunt-Väisälä frequency, S is the vertical wind shear, and the overbar denotes a moving average in 200-m step to eliminate the influence of small-scale fluctuations, such as turbulence and small-scale waves. In this case, the matching quantities that include *Ri*, wind shear, and the Brunt-Väisälä frequency between radiosonde and ERA5 profiles are actually handled in averaged 200 m intervals. The occurrence frequency of KHI is defined as the ratio of $Ri<1/4$ relative to all *Ri* calculations at a specified time period or height interval.

In Eq.(1), the length scale of overbar could potentially impact the value of *Ri*, and

https://doi.org/10.5194/acp-2022-851
Preprint. Discussion started: 20 February 2023

eventually, the occurrence frequency of KHI. In addition, the critical value of Ri and the vertical resolution of archived radiosonde could also cause the change in Ri values. We resample the HVRRS data to 50 m and 100 m, and range the length scale of overbar from 100 m to 500 m, to diagnose the uncertainties raised by the length scale of segments and the vertical resolution of dataset. As indicated in Figure 1, under the same length scale of overbar, a sparser vertical grid inevitably leads to a lower occurrence frequency of KHI. For instance, as the length scale set to 100 m, the occurrence frequency of Ri<1/4 at 0–2 km above sea level (a.s.l) decreases from 22% when vertical resolution is equal to 10 m to 16% for a vertical resolution of 50 m. Moreover, a longer length-scale of segment generally yields a smaller occurrence frequency. For example, as the vertical resolution of radiosonde is equal to 10 m, the occurrence frequency at 10–15 km decreases from 9% when the length scale of segment equals 100 m to 1% when it equals 500 m. It is interesting to note that the occurrence frequency under a vertical resolution of 50 m and a segment interval of 100 m is a bit larger than that under a vertical resolution of 10 m and a segment of 200 m, possibly implying the fact that a shorter segment interval could be expected for a sparser vertical resolution.

2.4 Gravity wave energy

The GW energy is extracted based on the broad spectral method, according to Wang and Geller (2003). In this method, the magnitude of measured zonal wind (u), meridional wind (v), and temperature (T) consisting of background states (u_0, v_0 and T_0) that are determined by applying a second-order polynomial fit (Chen et al., 2018; Zhang et al., 2022) and perturbations. Therefore, total perturbations are derived as:

$$(u', v', T') = (\mathrm{u}, \mathrm{v}, \mathrm{T}) - (u_0, v_0, T_0) \qquad (2)$$

The perturbations could include measurement noises, KH waves, GWs, and planetary waves. Only the perturbations with vertical wavelengths of 0.3–6.9 km are considered as GWs (Wang and Geller, 2003). By applying this band-pass filter, the average gravity-wave kinetic energy per unit mass (energy density) and the average

https://doi.org/10.5194/acp-2022-851
Preprint. Discussion started: 20 February 2023

potential energy density can be expressed as:

$$E_k = \frac{1}{2}\left[\overline{u'^2} + \overline{v'^2}\right] \qquad (3)$$

$$E_p = \frac{1}{2}\frac{g^2\overline{\hat{T}'^2}}{N^2} \qquad (4)$$

where g is the gravitational constant, $\hat{T}' = T'/\bar{T}$ the normalized perturbation temperature, and the overbar indicates an averaging over the tropospheric segment, which is chosen as 2–8.9 km for all regions, expect the polar region, and it is selected as 2–7.4 km for the polar region (Wang and Geller, 2003). Eventually, the total GW energy E_t is the sum of E_k and E_p.

3 Results and Discussions

3.1 Comparisons of wind shear between HVRRS and ERA5 reanalysis

The variations in vertical shear of horizontal wind speed and the squared Brunt-väisälä frequency entirely determine the Ri magnitude. Figure 2 provides an overview of the spatial distribution of wind shear at heights of 0–2 km a.s.l and 10–15 km a.s.l obtained from the HVRRS and ERA5 reanalysis, explicitly representing the variations of shear in the planetary boundary layer (PBL) and the upper troposphere, respectively. The shear in the PBL regime estimated by ERA5 reanalysis demonstrates a strong spatial variation, and it is largely dependent on underlying terrains and latitudes (Fig.2a). For example, large values in the PBL regime can most likely be observed along the coastline, which could be attributed to the prevailing sea-breeze circulation. Large wind shear is common in regions where stability changes rapidly (Grasmick and Geerts, 2020). As compared to the HVRRS, these shears are slightly underestimated by approximately 4 m/s/km, mostly based on continental sounding measurements. However, the oceanic shear is hard to be quantitatively assessed by a large number of *in-situ* radiosonde stations, with this aspect likely being evaluated by the ship-based radiosonde. Over the tropical oceans, Savazzi et al. (2022) found the wind bias between EUREC^{4}A field campaign and the ERA5 reanalysis varies greatly from day to day, attributing to the bias in wind forecasting in the ERA5 reanalysis.

https://doi.org/10.5194/acp-2022-851
Preprint. Discussion started: 20 February 2023

Nevertheless, a close association between averaged ERA5-reterived shears and HVRRS-determined shears can be noticed in terms of geospatial distribution, with a correlation coefficient of 0.36.

It is noteworthy that shears in the ERA5 reanalysis at heights of 10–15 km a.s.l is dramatically underestimated by around 8 m/s/km, especially at middle latitudes, compared to the HVRRS. The underestimation could partly be due to the coarse vertical resolution (around 300-m) in the ERA5 reanalysis in this height interval. However, the spatial distribution of the ERA5 shear still exhibits a significant positive correlation with the HVRRS shear, with a correlation coefficient of 0.35 (Fig.2d).

Following Houchi et al. (2010), the monthly shears over seven typical climate zones are separately investigated, which are defined as follows: Northern Hemisphere/Southern Hemisphere polar (70°–90°), Northern Hemisphere/Southern Hemisphere midlatitude (40°–70°), Northern Hemisphere/Southern Hemisphere subtropics (20°–40°), and tropics (20°S–20°N). Over the polar region in the Northern/Southern Hemisphere, HVRRS-based shears are exceptionally strong in the lower stratosphere compared to those in the troposphere (Fig.3a, g), which could be attributed to the stratospheric polar jet. However, the similar altitude variation can hardly be found in ERA5-based shears that are dramatically underestimated by around 16 m/s/km in the lower stratosphere (Fig.3h, n). The results in midlatitudes reach a similar conclusion (Fig.3b, f, i, m). Over subtropical regions in the Northern/Southern Hemisphere, HVRRS-based shears are consistent strong at heights of 16–21 km a.s.l, just above the subtropical jet stream (Fig.3c, e). However, in the ERA5 reanalysis, the region with consistently strong shears can be noticed at approximately 16 km a.s.l (Fig.3j, l), which is about 3 km lower than that in the HVRRS. In the tropics, the signature of quasi-biennial oscillation (QBO) can be identified in the lower stratosphere (Fig.3d, k).

Overall, the ERA5-based shears are underestimated at almost all investigated heights and over all climate zones, especially in the lower stratosphere. The comparison between HVRRS-based and ERA5-based shears at three typical regimes are tabulated in Table 1, representing the comparison result in the PBL region, the

https://doi.org/10.5194/acp-2022-851
Preprint. Discussion started: 20 February 2023

middle and upper troposphere, and the lower stratosphere. These metrics highlight that ERA5-based shears are underestimated by approximately 5 m/s/km, 7.5 m/s/km, 10 m/s/km at heights of 0–2 km, 10–15 km, and 20–25 km a.s.l, respectively, which are roughly consistent with Houchi et al. (2010).

By comparison, the ERA5-acquired N^2 averaged from the surface to 30 km a.g.l is reliably estimated over all climate zones, with a relative error of around 14%, as illustrated in Figure S3. This finding indicates that the ERA5 reanalysis can properly present the static stability of the background atmosphere, but it is not properly coincident with radiosonde in terms of the small-scale variability of dynamical structures. Due to a lack of global measurement of the fine-structure of the upper-air wind, however, the accuracy of ERA5-resolved shears is hard to be globally validated.

3.2 Occurrence frequency of *Ri*<1/4 in HVRRS and ERA5 reanalysis

As a prominent example, the monthly occurrence frequency of *Ri*<1/4 over the Corpus Christi station (27.77 ° N, −97.5 ° W) during years from January 2017 to October 2022 is illustrated in Figure 4. As a result, the monthly occurrence rate of *Ri*<1/4 in the PBL regime determined from HVRRS is lower than the ERA5-based one, with mean values of around 10.6% and 16.9%, respectively. In the lowermost 2 km, the vertical resolution of ERA5 reanalysis is less than 200 m, and it is less than the moving segment interval in Eq.(1). The high occurrence frequency in the PBL regime could be likely related to the convective activity that leads to a negative N^2. Especially during the daytime, PBL is well mixed due to strong turbulence induced by uprising thermals (Song et al., 2018). In addition, an obvious seasonal cycle of occurrence frequencies is revealed by HVRRS in the middle and upper troposphere and has a maximal in the spring season (March–April–May), which is consistent with the finding in Zhang et al. (2019). In the vicinity of jet streams, the occurrence frequency of *Ri*<1/4 is generally enhanced by large wind shears. However, the ERA5 reanalysis is hard to provide such a seasonal cycle pattern, and it is significantly underestimated by around 8%, which could be attributed to the underestimation in

https://doi.org/10.5194/acp-2022-851
Preprint. Discussion started: 20 February 2023

wind shears. In the lower stratosphere, both the HVRRS and ERA5 reanalysis provide a low estimation of occurrence frequencies, with a value of around 1%.

Furthermore, on a large spatial scale the occurrence frequency of $Ri<1/4$ retrieved by ERA5 reanalysis is remarkably underestimated in the free atmosphere, as compared to the HVRRS. The annual variation of the occurrence frequency of $Ri<1/4$ over seven climate zones at 0 to 30 km a.g.l indicated by HVRRS and ERA5 reanalysis is further demonstrated in Figure 5. It is clearly seen that the occurrence frequency of $Ri<1/4$ provided by ERA5 reanalysis is underestimated in all months, over all climate zones, possibly implying that, in the free atmosphere, the threshold value of 1/4 in Eq.(1) is too small for the ERA5 reanalysis to capture the occurrence of KHI.

Therefore, the question posed here is, what is the proper threshold value of *Ri* in predicting the occurrence of KHI when using the ERA5 reanalysis? The occurrence frequency of $Ri<1/4$ indicated by the HVRRS, the ERA5-determined occurrence frequencies produced by $Ri<0.25$, $Ri<0.5$, $Ri<1$, $Ri<1.5$, and $Ri<2$ at all heights up to 30 km a.s.l are demonstrated in Figure 6. It is notable that over all climate zones and in the free atmosphere, occurrence frequencies of $Ri<0.25$ and $Ri<0.5$ obtained from the ERA5 reanalysis are undervalued, but the frequencies of $Ri<1.5$ and $Ri<2$ are generally overvalued. Among others, the occurrence frequency of $Ri<1$ gives a close estimation both in magnitude and spatial variation compared to HVRRS over all climate zones.

Furthermore, the correlation coefficients between HVRRS-determined KHI occurrence frequency and the ERA5-determined frequencies indicated by different threshold values of *Ri* at height levels of 0 to 30 km are illustrated in Figure 7. It is worth noting that, in the troposphere, the ERA5-based frequencies indicated by $Ri<1$, $Ri<1.5$, and $Ri<2$ are highly positively correlated with those from the HVRRS, with a correlation coefficient of around 0.6 over all climate zones. In the lower stratosphere, however, these coefficients rapidly decline to 0.1, which can be explained by the low occurrence frequency of KHI in this height regime.

Combined the findings in Figures 6 and 7, in the free troposphere, we can

https://doi.org/10.5194/acp-2022-851
Preprint. Discussion started: 20 February 2023

conclude that the ERA5-determined occurrence frequency of $Ri<1$ is closest to the frequency of $Ri<1/4$ based on the HVRRS. In the free atmosphere, KHI is the dominant source for clear-air turbulence (CAT) that is a well-known hazard to aviation. Therefore, the global characterization of KHI occurrence frequency in the free atmosphere obtained from ERA5 reanalysis could be of importance for understanding the spatial-temporal variation of CAT. In the following sections, the occurrence frequency of KHI (hereinafter *OF*(KHI)) is based on $Ri<1$ in ERA5 reanalysis and $Ri<1/4$ in HVRRS, unless otherwise noted.

3.3 The *OF*(KHI) climatology

For a first hint the global distributions of *OF*(KHI) provided by the ERA5 reanalysis at 0–2 km a.s.l and 10–15 km a.s.l are displayed in Figure 8. *OF*(KHI) in the PBL region is considerably spatially heterogeneous. Over subtropical oceans in the Northern/Southern Hemisphere, the intense *OF*(KHI) can be noticed and has a magnitude of around 50% (Fig.8a). In addition, over the Sahara Desert the *OF*(KHI) reaches as high as 65%. Interestingly, the spatial variation in *OF*(KHI) keeps high consistency with that of planetary boundary layer height (PBLH), as shown in Figure S4. Usually, in the PBL regime, a deeper PBLH that represents more vigorous convection activities can predict a higher *OF*(KHI). These findings suggest that, in the PBL regime, the burst of KHI is likely closely associated with thermal convection due to the heating of the ground. Similarly, at heights of 10–15 km a.s.l, intensive *OF*(KHI) can be viewed over subtropic regions and has a value of around 10% (Fig.8b), which is likely attributed to upper tropospheric jets.

In comparison, the spatial-temporal variability of *OF*(KHI) indicated by HVRRS keeps high consistency with that of ERA5 reanalysis over all climate zones and at all heights up to 30 km (Figure 9), especially in the free troposphere. Obvious seasonal cycles can be detected over subtropics and midlatitude regions in the troposphere by both the HVRRS and ERA5 reanalysis. However, the ERA5-based *OF*(KHI) can only reflect the backbone of the cycles, and it is hard to quantify the detailed variation like

https://doi.org/10.5194/acp-2022-851
Preprint. Discussion started: 20 February 2023

Atmospheric Chemistry and Physics Discussions

the HVRRS does. For regions without high-resolved wind and temperature measurements, the ERA5 model product could be a good choice to represent the thermodynamic instability of background atmosphere. Although ERA5-based *OF*(KHI) is consistent with the HVRRS-based one from a global perspective, it is generally underestimated over polar regions (Fig.9a, g, h, n).

Furthermore, the seasonal variation of *OF*(KHI) over seven climate zones indicated by two datasets is shown in Figure 10. Over midlatitude and subtropics regions, the *OF*(KHI) quickly decreases from around 40% in the PBL regime to around 6% at around 3 km and then increases to around 8% at around 9 km, and eventually, it decreases to around 2% in the lower stratosphere (Fig.10b,c,e,f). Over tropic regions, a primary peak can be clearly noticed at around 13 km, with a maximum of 12% for the HVRRS and 20% for the ERA5 reanalysis (Fig.10d, k). Over polar regions, the tropospheric *OF*(KHI) is significantly lower than that over other climate zones, with values ranging from around 4% at heights of 2–8 km to 1% in the lower stratosphere (Fig.10a,g).

As well, the latitude-altitude variation of ERA5-reterived *OF*(KHI) is clearly notable. In the free atmosphere the highest occurrences can be noticed at height intervals of 8–15 km over tropical zones in all seasons, with magnitudes of around 30%. A poleward decrease pattern can be clearly detected in all seasons, with values varying from 30% at low latitudes to around 5% at high latitude in the middle and upper troposphere, which is consistent with the report in Zhang et al. (2022).

In Table 2, the mean *OF*(KHI) magnitudes over seven climate zones and at three typical altitude regimes are listed. In the PBL, the ERA5-based *OF*(KHI) is about 20% larger than that of the HVRRS-based one. In the middle and upper stratosphere, the ERA5-based *OF*(KHI) is reasonably well estimated, except that it is overestimated by around 5.8% over the tropics region. In addition, ERA5 underestimates *OF*(KHI) by around 0.5% in the lower stratosphere.

According to Fig.8a, it seems that low-level *OF*(KHI) is dependent on underlying terrains. Therefore, we investigate the association of low-level HVRRS-determined *OF*(KHI) with the standard deviation of orography (SDOR). At heights of 1–2 km

https://doi.org/10.5194/acp-2022-851
Preprint. Discussion started: 20 February 2023

a.g.l, the underlying terrain with a large SDOR generally corresponds to a high *OF*(KHI), with a correlation coefficient between *OF*(KHI) and SDOR of 0.24. Then, the coefficient decreases to 0.15 at 3–4 km a.g.l (Fig.11b), and eventually, it equals 0.14 at 5–6 km a.g.l (Fig.11c). These findings indicate that, over mountainous areas, a high low-level *OF*(KHI) would be expected.

Moreover, it is quite evident from Fig.8b that the *OF*(KHI) is largely enhanced over the tropical ocean associated with El Niño Southern Oscillation (ENSO) events. The most of the enhanced *OF*(KHI) can be identified over the Niño 3 region (5 °N–5 °S, 150 ° W–90 ° W), and the time-height cross section of *OF*(KHI) during years of 2000 to 2022 is illustrated in Figure 12. The *OF*(KHI) at height region of 6–13 km are evidently large, with values of around 40%, which is about 20% larger than the climatological mean value (Fig.9j). More specifically, *OF*(KHI) during time periods of La Niño events is obviously stronger than that during the EI Niño periods. The identification of ENSO events is based on Ren et al. (2018), Li et al. (2022), and Lv et al. (2022). It is also worth recalling here that the wind shear does not exhibit such an anomaly over the Niño 3 region (Fig.2c), implying that the *OF*(KHI) anomaly could likely be attributed to the ENSO-related tropical convective heating in the upper troposphere.

3.4 The dynamical environment of KHI

In the PBL, the raised KHI could be attributed to the interaction between complex terrain and low-level wind and thermal convection. While in the free atmosphere where the convection activity is weak, KHI is preferentially generated from strong wind shear, which is closely associated with mean flows and wave activities.

We first evaluate the association of low-level *OF*(KHI) with near-surface wind speed for the HVRRS station with a SDOR greater than 50 (Figure 13). It is probably not surprising that the *OF*(KHI) is positively correlated with near-surface wind speed at both heights of 1–2 km and 3–4 km a.g.l, with correlation coefficients of 0.09 and 0.04, respectively. These low coefficients could be attributed to too large samples.

https://doi.org/10.5194/acp-2022-851
Preprint. Discussion started: 20 February 2023

Therefore, we infer that the interaction between near-surface winds and complex terrains could increase the magnitude of low-level *OF*(KHI).

The propagation of GW could raise strong wind shear, and therefore generate KHI. Thereby, we investigate the joint distribution of *OF*(KHI) with tropospheric GW total energy and wind shear (Figure 14). The latitudinal variation of GW total energy exhibits a double-peak structure, with two peaks at around 30° in the Northern/Southern Hemisphere (Fig.14a). Overall, large *OF*(KHI) always corresponds to strong GW activities and large wind shears, likely indicating that GW activity is crucial for the occurrence of KHI.

In addition, the interaction between low-level wind and mountain barrier could be a source of orographic GWs (Zhang et al., 2022). We take orographic GW dissipation in ERA5 reanalysis, which is the accumulated conversion of kinetic energy in the mean flow into heat over the whole atmospheric column, as an indicator of the strength of orographic GWs. It is interesting to note that monthly averaged orographic GW dissipation and ERA5-determined *OF*(KHI) at heights from ground up to 30 km demonstrates a close association (Figure S5). For instance, in the middle troposphere, they are positively associated over mountainous areas such as the Rocky Mountains and the Alps Mountain, with correlation coefficients of around 0.5. These findings also suggest that the propagation of orographic GWs could be a potential source for KHI.

At jet heights (10–15 km a.g.l), a large shear is easily induced by strong wind speed. Figure 15 demonstrates the joint distribution of *OF*(KHI) with wind speed and wind shear. Similarly, large *OF*(KHI) can be easily found when the wind speed exceeds 20 m/s and wind shear is larger than 20 m/s/km. However, it is clear that large wind speed is not a necessary condition for KHI. The occurrence of KHI favors the mean flow with a speed exceeding 20 m/s, but it does not ensure to happen for an extremely large wind speed.

In a short conclusion, in the troposphere, the occurrence of KHI favors the dynamical environment with strong orographic or non-orographic GW activities and relatively large mean flow (>20 m/s).

https://doi.org/10.5194/acp-2022-851
Preprint. Discussion started: 20 February 2023

4 Conclusion and remarks

The occurrence of KHI is potential crucial for many implications, such as aircraft, mass transfer, and climate change, just name a few, but it is very hard to be globally understood due to its fine structure. This analysis uses high-resolution model products and radiosondes to globally characterize the distribution of KHI occurrence frequency from the years 2017 to 2022.

Wind shears are considerably underestimated at almost all heights and over all climate zones by the ERA5 reanalysis, compared to the HVRRS. It is noteworthy that shears in the ERA5 reanalysis at heights of 10–15 km a.s.l is dramatically underestimated by around 8 m/s/km, especially at middle latitudes. However, the spatial distribution of the ERA5 shear exhibits a statistically significant positive correlation with the HVRRS shear. The underestimation therefore influences the performance of KHI analysis. As a result, the ERA5-determined occurrence frequency of $Ri<1/4$ in the free tropospheric is significantly underestimated. In addition, it is poorly correlated with HVRRS-determined ones at all heights and over all climate zones.

Interestingly, the ERA5-determined occurrence frequency of $Ri<1$ is highly consistent with the frequency of $Ri<1/4$ obtained from HVRRS, in terms of magnitude and temporal variation. Rather than $Ri<1/4$, the threshold value of $Ri<1$ could be more proper when using ERA5 reanalysis for KHI study, especially in the middle and upper troposphere over midlatitude and subtropic regions in the Northern/Southern Hemisphere.

The climatology of *OF*(KHI) exhibits significant seasonal cycles over polar, midlatitude, and subtropic regions. A poleward decrease can be clearly identified in the middle and upper troposphere. In addition, the low-level *OF*(KHI) is positively sensitive to the standard deviations of orography. Moreover, it is immediately obvious that the *OF*(KHI) in the middle and upper troposphere of the Niño 3 region is largely enhanced by the tropical convective heating.

https://doi.org/10.5194/acp-2022-851
Preprint. Discussion started: 20 February 2023

Atmospheric Chemistry and Physics Discussions

Over the mountainous area, the low-level *OF*(KHI) favors large near-surface wind speed. In the free troposphere, the *OF*(KHI) favors intensive orographic or non-orographic GW activities and relatively large mean flow (>20 m/s).

Those findings could be valuable for pointing out the performance of ERA5 reanalysis in terms of representing KHI occurrence frequency, as compared to a near-global high-resolution radiosonde measurement. In addition, the spatial-temporal variability of *OF*(KHI) over different climate zones from near-ground up to 30 km is quantitatively characterized, which could provide new insights that increase our understanding of the fine structure of upper air.

Acknowledgement

The authors would like to acknowledge the National Meteorological Information Centre (NMIC) of CMA, NOAA, Deutscher Wetterdienst (Climate Data Center), U.K Centre for Environmental Data Analysis (CEDA), GRUAN, ECMWF, and the University of Wyoming for continuously collecting and generously providing high-resolution radiosonde data.

Financial support

This study jointly supported by the National Natural Science Foundation of China under grants 42205074, 42127805, and 62101203, and the Research Grants of Huazhong Agricultural University under grants No. 2662021XXQD002 and 2662021JC008.

https://doi.org/10.5194/acp-2022-851
Preprint. Discussion started: 20 February 2023

Atmospheric Chemistry and Physics Discussions

Competing interests

The contact author has declared that neither they nor their co-authors have any competing interests

Data availability

The dataset can be accessed at ECMWF (2022).

Author contributions

JZ conceptualized this study. JS carried out the analysis with comments from other co-authors. JZ wrote the original manuscript. WW, SZ, TY, WD provided useful suggestions for the study. All authors contributed to the improvement of paper.

References

Baumgarten, G., and Fritts, D. C.: Quantifying Kelvin-Helmholtz instability dynamics observed in noctilucent clouds: 1. Methods and observations, J. Geophys. Res. Atmos., 119, 9324–9337, https://doi.org/10.1002/2014JD021832, 2014.

Duruisseau, F., N., Huret, A., Andral, and Camy-Peyret, C.: Assessment of the ERA-Interim winds using high-altitude stratospheric balloons, J. Atmos. Sci., 74(6), 2065–2080, https://doi.org/10.1175/JAS-D-16-0137.1, 2017.

Dong, W., Fritts, D. C., Lund, T. S., Scott, A.W., and Zhang, S: Self-acceleration and Instability of Gravity Wave Packets: 2. Two-Dimensional Packet Propagation, Instability Dynamics, and Transient Flow Responses, J. Geophys. Res. Atmos., https://doi.org/10.1029/2019JD030691, 2020.

Dong, W., Fritts, D. C., Thomas, G. E., and Lund, T. S.: Modeling responses of polar mesospheric clouds to gravity wave and instability dynamics and induced large-scale motions, J. Geophys. Res. Atmos., 126, e2021JD034643. https://doi.org/10.1029/2021JD034643, 2021.

Dong, W., Fritts, D. C., Hickey, M. P., Liu, A. Z., Lund, T. S., Zhang, S., et al.: Modeling studies of gravity wave dynamics in highly structured environments: Reflection, trapping, instability, momentum transport, secondary gravity waves, and induced flow responses, J. Geophys. Res. Atmos., 127, e2021JD035894. https://doi.org/10.1029/2021JD035894, 2022.

ECMWF: ECMWF Reanalysis v5 (ERA5), European Centre for Medium-Range Weather Forecasts [data set], https://www.ecmwf.int/en/forecasts/dataset/ecmwf-reanalysis-v5, last access: 07 December 2022.

Fritts, D. C., K. Wan, J. Werne, T. Lund, and Hecht, J. H.: Modeling the implications of Kelvin-Helmholtz instability dynamics for airglow observations, J. Geophys. Res. Atmos., 119, 8858–8871, https://doi.org/10.1002/2014JD021737, 2014.

Fritts, D. C., P. M. Franke, K. Wan, T. Lund, and Werne, J.: Computation of clear-air radar backscatter from numerical simulations of turbulence: 2. Backscatter moments throughout the lifecycle of a Kelvin Helmholtz instability, J. Geophys. Res., 116, D11105, https://doi.org/10.1029/2010JD014618, 2011.

Fritts, D. C., and Rastogi, P. K.: Convective and dynamical instabilities due to gravity wave motions in the lower and middle atmosphere: Theory and observations. Radio Sci., 20, 1247–1277, https://doi.org/10.1029/RS020i006p01247, 1985.

Fritts, D. C., L., Wang, T. S., Lund, S. A., Thorpe, C. B., Kjellstrand, B., Kaifler, and Kaifler, N.: Multi-Scale Kelvin-Helmholtz instability dynamics observed by PMC Turbo on 12 July 2018: 2. DNS modeling of KHI dynamics and PMC responses., J. Geophys. Res. Atmos., 127, e2021JD035834. https://doi.org/10.1029/2021JD035834, 2022.

Fritts, D. C., Dong, W., Lund, T. S., and Brain., L.: Self-Acceleration and Instability

https://doi.org/10.5194/acp-2022-851
Preprint. Discussion started: 20 February 2023

Atmospheric Chemistry and Physics
Discussions

of Gravity Wave Packets: 3. Three-Dimensional Packet Propagation, Secondary Gravity Waves, Momentum Transport, and Transient Mean Forcing in Tidal Winds, J. Geophys. Res. Atmos., https://doi.org/10.1029/2019JD030692, 2020.

Grasmick, C., and Geerts, B.: Detailed dual-Doppler structure of Kelvin–Helmholtz waves from an airborne profiling radar over complex terrain. Part I: Dynamic structure, J. Atmos. Sci., 77(5), 1761–1782., https://doi.org/10.1175/JAS-D-19-0108.1, 2020.

Gavrilov, N. M., Luce, H., Crochet, M., Dalaudier, F., and Fukao, S.: Turbulence parameter estimations from high-resolution balloon temperature measurements of the MUTSI-2000 campaign, Ann. Geophys., 23, 2401–2413, doi:10.5194/angeo-23-2401-2005, 2005

Guo, J., Zhang, J., Yang, K., Liao, H., Zhang, S., Huang, K., Lv, Y., Shao, J., Yu, T., Tong, B., Li, J., Su, T., Yim, S. H. L., Stoffelen, A., Zhai, P., and Xu, X.: Investigation of near-global daytime boundary layer height using high-resolution radiosondes: first results and comparison with ERA5, MERRA-2, JRA-55, and NCEP-2 reanalyses, Atmos. Chem. Phys., 21, 17079–17097, https://doi.org/10.5194/acp-21-17079-2021, 2021.

Haack, A., M. Gerding, and Lübken, F.-J.: Characteristics of stratospheric turbulent layers measured by LITOS and their relation to the Richardson number, J. Geophys. Res. Atmos., 119, 10605–10618, https://doi.org/10.1002/2013JD021008, 2014.

Hersbach, H., Bell, B., Berrisford, P., Hirahara, S., Horányi, A., Muñoz-Sabater, J., Nicolas, J., Peubey, C., Radu, R., Schepers, D., Simmons, A., Soci, C., Abdalla, S., Abellan, X., Balsamo, G., Bechtold, P., Biavati, G., Bidlot, J., Bonavita, M., De Chiara, G., Dahlgren, P., Dee, D., Diamantakis, M., Dragani, R., Flemming, J., Forbes, R., Fuentes, M., Geer, A., Haimberger, L., Healy, S., Hogan, R. J., Hólm, E., Janisková, M., Keeley, S., Laloyaux, P., Lopez, P., Lupu, C., Radnoti, G., de Rosnay, P., Rozum, I., Vamborg, F., Villaume, S., and Thépaut, J.-N.: The ERA5 global reanalysis, Q. J. Roy. Meteorol. Soc., 146, 1999–2049,

https://doi.org/10.5194/acp-2022-851
Preprint. Discussion started: 20 February 2023

Atmospheric Chemistry and Physics Discussions

https://doi.org/10.1002/qj.3803, 2020.

Homeyer, C. R., L. L. Pan, and Barth, M. C.: Transport from convective overshooting of the extratropical tropopause and the role of large-scale lower stratospheric stability, J. Geophys. Res. Atmos., 119(5), 2220–2240, https://doi.org/10.1002/2013JD020931, 2014.

Houchi, K., Stoffelen, A., Marseille, G. J., and De Kloe, J.: Comparison of wind and wind shear climatologies derived from high-resolution radiosondes and the ECMWF model, J. Geophys. Res.-Atmos., 115, D22123, https://doi.org/10.1029/2009JD013196, 2010.

Li, X., Hu, Z. Z., Tseng, Y. H., Liu, Y., and Liang, P.: A historical perspective of the La Niña event in 2020/2021, J. Geophys. Res.-Atmos., 127(7), e2021JD035546, https://doi.org/10.1029/2021JD035546, 2022.

Lv, A., Fan, L., and Zhang, W.: Impact of ENSO Events on Droughts in China, Atmosphere, 13(11), 1764, https://doi.org/10.3390/atmos13111764, 2022.

Jaeger, E. B., and Sprenger, M.: A Northern Hemispheric climatology of indices for clear air turbulence in the tropopause region derived from ERA40 reanalysis data, J. Geophys. Res., 112, D20106, doi:10.1029/2006JD008189, 2007.

Ko, H. C., H. Y., Chun, R., Wilson, and Geller, M. A.: Characteristics of atmospheric turbulence retrieved from high vertical-resolution radiosonde data in the United States, J. Geophys. Res. Atmos., 124.https://doi.org/10.1029/2019JD030287, 2019.

Ko, H. C. and Chun, H. Y.: Potential sources of atmospheric turbulence estimated using the Thorpe method and operational radiosonde data in the United States. Atmos. Res., 265, 105891, https://doi.org/10.1016/j.atmosres.2021.105891, 2022.

Muschinski, A., and Wode, C.: First in situ evidence for coexisting submeter temperature and humidity sheets in the lower free troposphere, J. Atmos. Sci., 55(18), 2893–2906, https://doi.org/10.1175/1520-0469(1998)055<2893:FISEFC>2.0.CO;2, 1998.

Plougonven, R., and Zhang, F.: Internal gravity waves from atmospheric jets and

https://doi.org/10.5194/acp-2022-851
Preprint. Discussion started: 20 February 2023

fronts, Rev. Geophys., *52*, 33–76, https://doi.org/10.1002/2012RG000419, 2014.

Rennie, M. P., Isaksen, L., Weiler, F., de Kloe, J., Kanitz, T., and Reitebuch, O.: The impact of Aeolus wind retrievals on ECMWF global weather forecasts, Q. J. Roy. Meteorol. Soc., 147(740), 3555–3586, https://doi.org/10.1002/qj.4142, 2021.

Ren, H. L., B., Lu, J., Wan, B., Tian, and Zhang, P.: Identification standard for ENSO events and its application to climate monitoring and prediction in China, J. Meteorol. Res., 32, 923–936, https://doi.org/10.1007/s13351-018-8078-6, 2018.

Sandu, I., A., A., van Niekerk, T. G., Shepherd, S. B., Vosper, A., Zadra, J., Bacmeister, et al: Impacts of orography on large-scale atmospheric circulation. npj Clim Atmos Sci, 2(1), 1–8, https://doi.org/10.1038/s41612-019-0065-9, 2019.

Savazzi, A. C. M., Nuijens, L., Sandu, I., George, G., and Bechtold, P.: The representation of the trade winds in ECMWF forecasts and reanalyses during EUREC^{4}A, Atmos. Chem. Phys., 22, 13049–13066, https://doi.org/10.5194/acp-22-13049-2022, 2022.

Sharman, R. D., S. B. Trier, T. P. Lane, and Doyle., J. D.: Sources and dynamics of turbulence in the upper troposphere and lower stratosphere: A review, Geophys. Res. Lett., 39, L12803, https://doi.org/10.1029/2012GL051996, 2012.

Song, J., Z.-H., Wang, and Wang, C.: The regional impact of urban heat mitigation strategies on planetary boundary layer dynamics over a semiarid city, J. Geophys. Res. Atmos., 123(12), 6410–6422, https://doi.org/10.1029/2018JD028302, 2018.

Sun, J., C. J., Nappo, L., Mahrt, D., Belušic, B., Grisogono, D. R., Stauffer, et al.: Review of wave-turbulence interactions in the stable atmospheric boundary layer, Rev. Geophys., *53*, 956–993, https://doi.org/10.1002/2015RG000487, 2015.

Wang, L., and Geller, M. A.: Morphology of gravity-wave energy as observed from 4 years (1998–2001) of high vertical resolution U.S. radiosonde data, J. Geophys. Res. Atmos., 108(D16), 4489, https://doi.org/10.1029/2002JD002786, 2003.

Williams, P. D., and Joshi, M. M.: Intensification of winter transatlantic aviation turbulence in response to climate change. Nat. Clim. Chang., 3(7), 644–648, https://doi.org/10.1038/nclimate1866, 2013.

Xia, P., Y., Shan, S., Ye, and Jiang, W.: Identification of Tropopause Height with Atmospheric Refractivity, J. Atmos. Sci., 78(1), 3–16 https://doi.org/10.1175/JAS-D-20-0009.1, 2021.

Zhang, J., S. D., Zhang, C. M., Huang, K. M., Huang, Y., Gong, Q., Gan, and Zhang, Y. H.: Latitudinal and topographical variabilities of free atmospheric turbulence from high-resolution radiosonde data sets, J. Geophys. Res. Atmos., 124, 4283–4298. https://doi.org/10.1029/2018JD029982, 2019.

Zhang, J., J., Guo, H., Xue, S., Zhang, K., Huang, W. Dong, et al.: Tropospheric gravity waves as observed by the high-resolution China radiosonde network and their potential sources, J. Geophys. Res. Atmos., 127, e2022JD037174, https://doi.org/10.1029/2022JD037174, 2022.

Zhang, J., J., Guo, S., Zhang, and Shao, J.: Inertia-gravity wave energy and instability drive turbulence: Evidence from a near-global high-resolution radiosonde dataset, Clim. Dyn., 58(11), 2927–2939, https://doi.org/10.1007/s00382-021-06075-2, 2022.

https://doi.org/10.5194/acp-2022-851
Preprint. Discussion started: 20 February 2023

Atmospheric Chemistry and Physics Discussions

Table 1. Comparisons of mean wind shears between HVRRS and ERA5 reanalysis at heights of 0–2 km a.s.l (a), 10–15 km a.s.l (b), and 20–25 km a.s.l (c).

(a) Wind shear at 0–2 km a.s.l (m/s/km)							
	Polar (NH)	**Midlatitude (NH)**	**Subtropics (NH)**	**Tropics**	**Subtropics (SH)**	**Midlatitude (SH)**	**Polar (SH)**
HVRRS	12.67	12.94	12.30	10.57	13.03	14.16	15.01
ERA5	7.45	7.68	7.78	5.4	8.44	9.67	8.42
(b) Wind shear at 10–15 km a.s.l (m/s/km)							
HVRRS	13.23	14.71	13.02	9.40	13.28	14.64	13.00
ERA5	4.22	6.13	6.82	5.86	6.86	5.20	3.42
(c) Wind shear at 20–25 km a.s.l (m/s/km)							
HVRRS	15.12	15.74	15.41	16.76	16.69	16.12	17.15
ERA5	2.87	3.52	4.06	5.27	3.99	3.36	2.92

https://doi.org/10.5194/acp-2022-851
Preprint. Discussion started: 20 February 2023

Atmospheric Chemistry and Physics Discussions

Table 2. Similar to Tab.1 but for the occurrence frequency of KHI. Note that the occurrence of KHI is indicated by Ri<1/4 in radiosonde, but it is identified with Ri<1 in ERA5 reanalysis.

(a) *OF*(KHI) at 0–2 km a.s.l (%)

	Polar (NH)	Midlatitude (NH)	Subtropics (NH)	Tropics	Subtropics (SH)	Midlatitude (SH)	Polar (SH)
HVRRS	9.56	16.10	15.78	13.08	16.98	15.38	13.97
ERA5	26.91	33.85	35.70	37.27	40.56	40.46	26.55

(b) *OF*(KHI) at 10–15 km a.s.l (%)

	Polar (NH)	Midlatitude (NH)	Subtropics (NH)	Tropics	Subtropics (SH)	Midlatitude (SH)	Polar (SH)
HVRRS	0.53	2.22	5.44	11.22	6.17	1.55	0.62
ERA5	0.44	2.62	6.86	17.03	7.15	1.67	0.28

(c) *OF*(KHI) at 20–25 km a.s.l (%)

	Polar (NH)	Midlatitude (NH)	Subtropics (NH)	Tropics	Subtropics (SH)	Midlatitude (SH)	Polar (SH)
HVRRS	0.36	0.49	0.43	0.5	0.40	0.67	1.35
ERA5	0.06	0.07	0.04	0.1	0.06	0.06	0.04

https://doi.org/10.5194/acp-2022-851
Preprint. Discussion started: 20 February 2023

Atmospheric Chemistry and Physics
Discussions

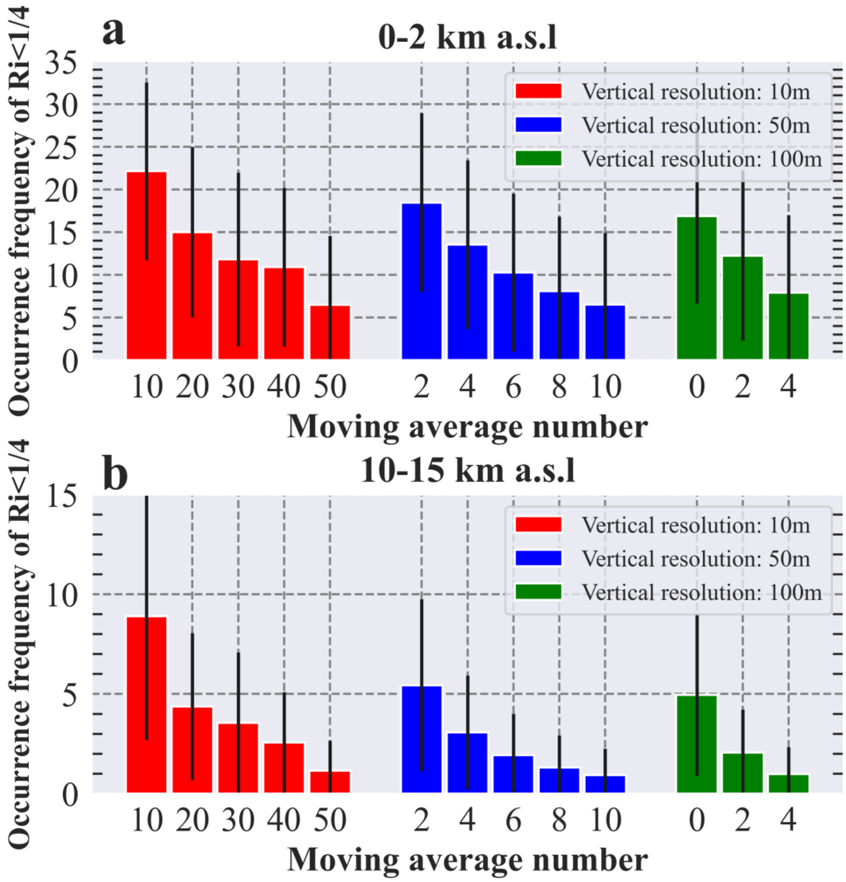

Figure 1. The averaged occurrence frequencies of Ri<1/4 at heights of 0–2 km a.s.l (a) and 10–15 km a.s.l (b), with vertical resolutions ranging 10-m to 100-m and moving point numbers increasing from 0 to 50. The error bars correspond to the standard deviation. The metrics are counted based on all radiosonde profiles during years 2017–2022.

https://doi.org/10.5194/acp-2022-851
Preprint. Discussion started: 20 February 2023

Atmospheric Chemistry and Physics
Discussions

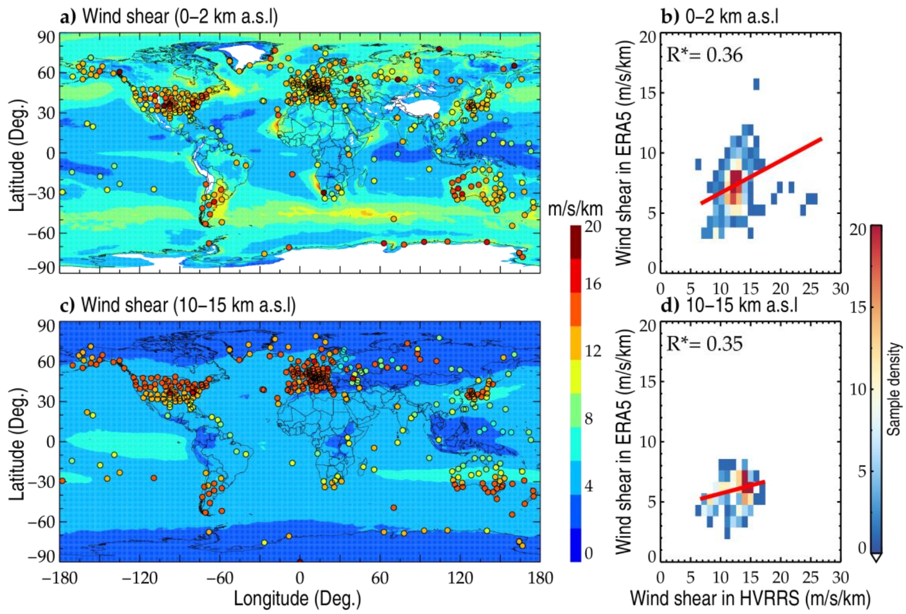

Figure 2. The spatial distribution of mean wind shear in ERA5 reanalysis at heights of 0–2 km a.s.l (a) and 10–15 km a.s.l (c), where the areas with a near-surface pressure lower than 800 hPa are masked with white. The overlaid colored circles represent the result in HVRRS at the same height levels. Each data point represents a vertically averaged value of the wind shear at one radiosonde station during the whole study period. Density plots (b, d) show the correlation between wind shears in HVRRS and ERA5 reanalysis. The ERA5 derived wind shears are spatially and temporally collocated with those of HVRRS. In addition, the red lines represent a least-squared linear regression, and the star superscripts indicate that values are statistically significant (p<0.05).

https://doi.org/10.5194/acp-2022-851
Preprint. Discussion started: 20 February 2023

Atmospheric Chemistry and Physics Discussions
Open Access
EGU

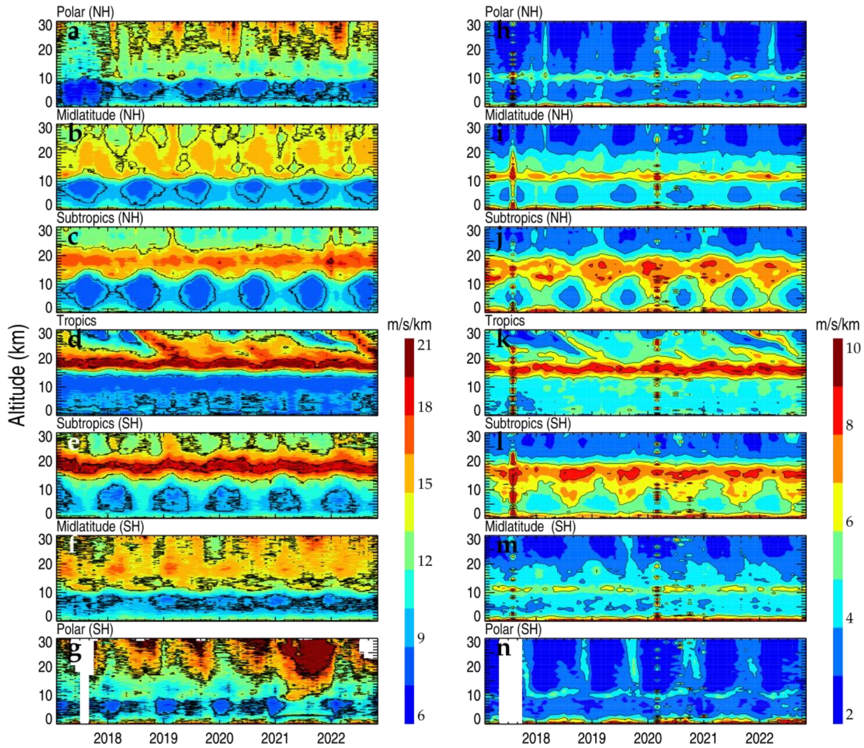

Figure 3. Monthly mean wind shears during years 2017–2022 in HVRRS (a–g) and ERA5 reanalysis (h–n) at different climate zones. The ERA5 derived wind shears are spatially and temporally collocated with those of HVRRS. NH=Northern Hemisphere; SH=Southern Hemisphere.

https://doi.org/10.5194/acp-2022-851
Preprint. Discussion started: 20 February 2023

Atmospheric Chemistry and Physics Discussions

732 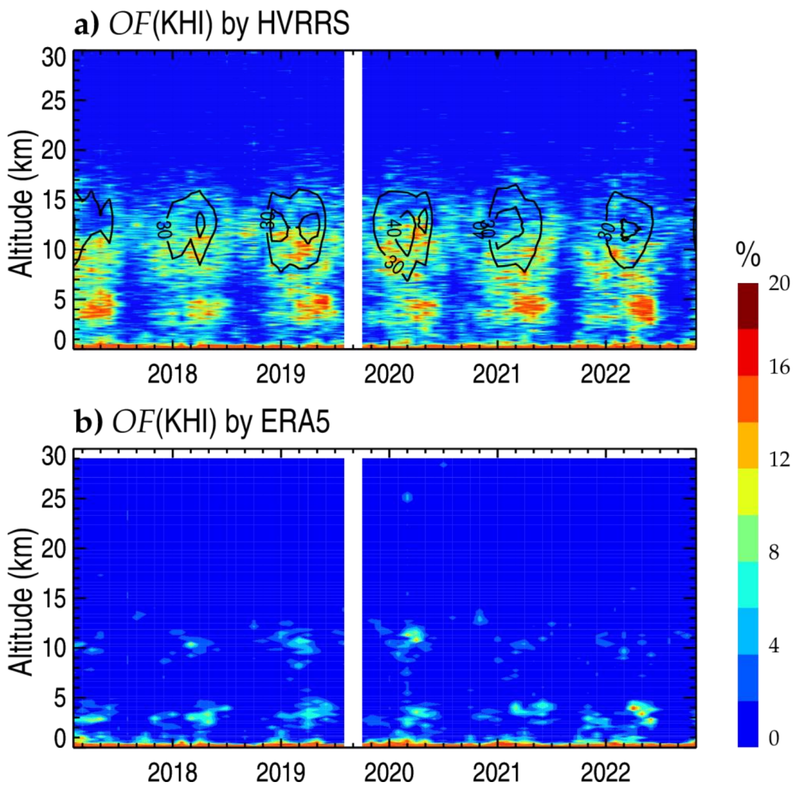

733 **Figure 4**. The monthly occurrence frequency of *Ri*<1/4 at Corpus Christi station
734 (27.77 °N, −97.5 °W) in HVRRS (a) and ERA5 reanalysis (b). Note that the contour
735 curves in (a) concern the mean horizontal wind speed, and that the ERA5 derived
736 quantities are spatially and temporally collocated with those of HVRRS.

https://doi.org/10.5194/acp-2022-851
Preprint. Discussion started: 20 February 2023

Atmospheric Chemistry and Physics Discussions

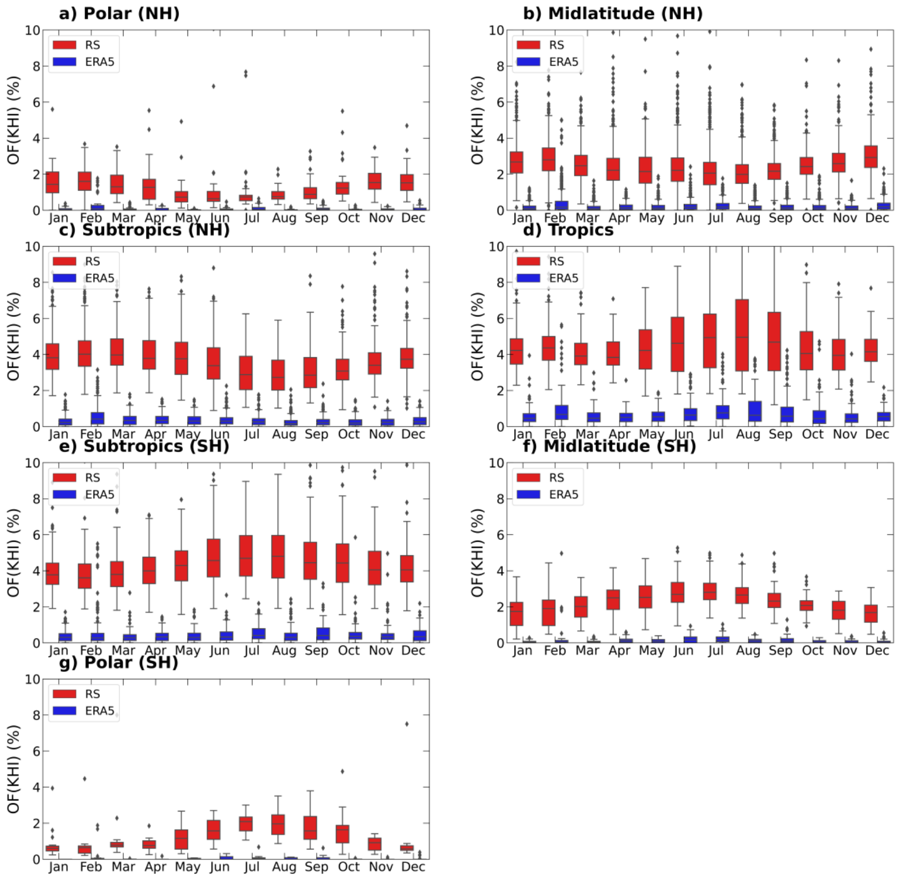

Figure 5. The annual cycles of the occurrence frequency of *Ri*<1/4 in different climate zones at 10–15 km a.s.l. The red and blue boxes represent the frequencies in HVRRS and ERA5 reanalysis, respectively. The ERA5 derived *Ri* is spatially and temporally collocated with that of HVRRS. NH, Northern Hemisphere; SH, Southern Hemisphere.

https://doi.org/10.5194/acp-2022-851
Preprint. Discussion started: 20 February 2023

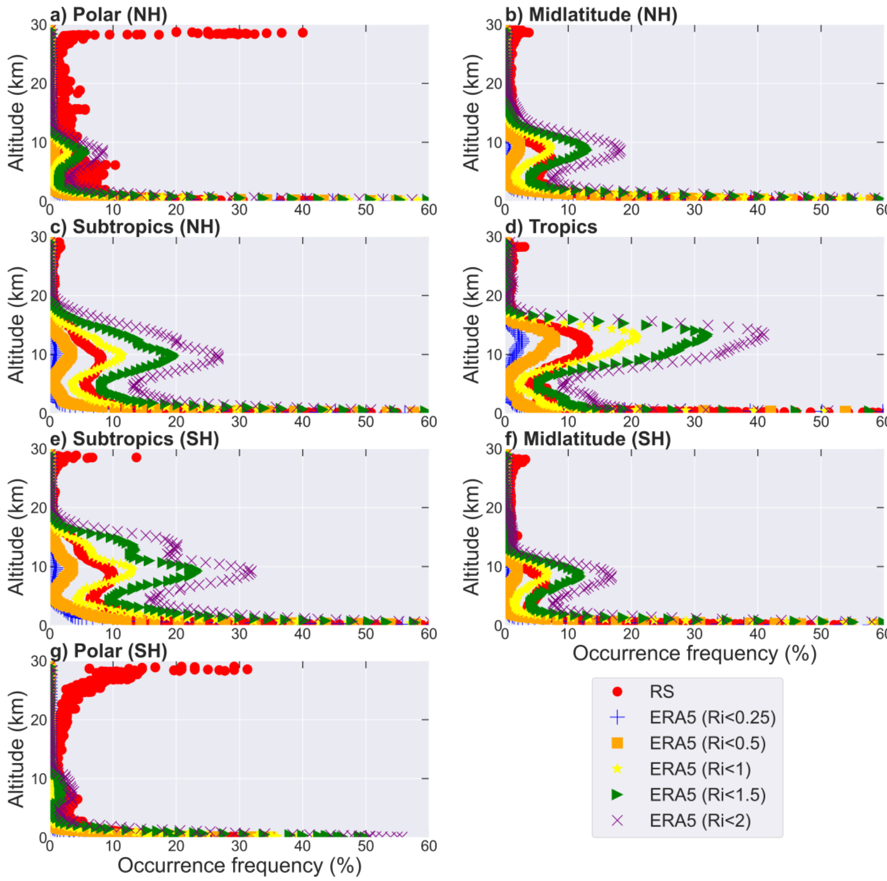

Figure 6. The altitude variation of the occurrence frequency of *Ri* below certain thresholds (0.25, 0.5, 1, 1.5, and 2) in ERA5 reanalysis in various climate zones. The ERA5 derived *Ri* is spatially and temporally collocated with that of HVRRS. The occurrences of *Ri*<1/4 in HVRRS are marked with red dots.

https://doi.org/10.5194/acp-2022-851
Preprint. Discussion started: 20 February 2023

Atmospheric Chemistry and Physics Discussions

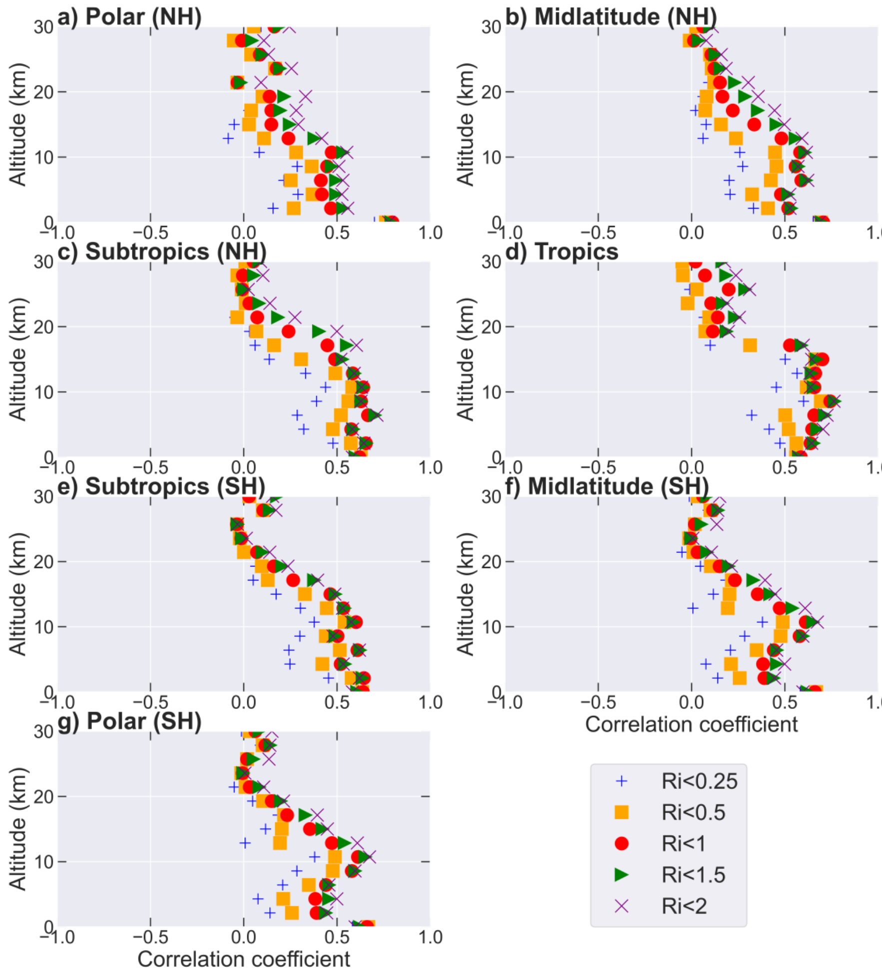

Figure 7. The correlation coefficients between monthly averaged KHI occurrence frequency in the HVRRS and the monthly occurrence frequency of *Ri* below certain thresholds (0.25, 0.5, 1, 1.5, and 2) in ERA5 reanalysis. The ERA5 derived *Ri* is spatially and temporally collocated with that of HVRRS. The coefficients in various climate zones are estimated in an increment of 2 km.

https://doi.org/10.5194/acp-2022-851
Preprint. Discussion started: 20 February 2023

Atmospheric Chemistry and Physics
Discussions

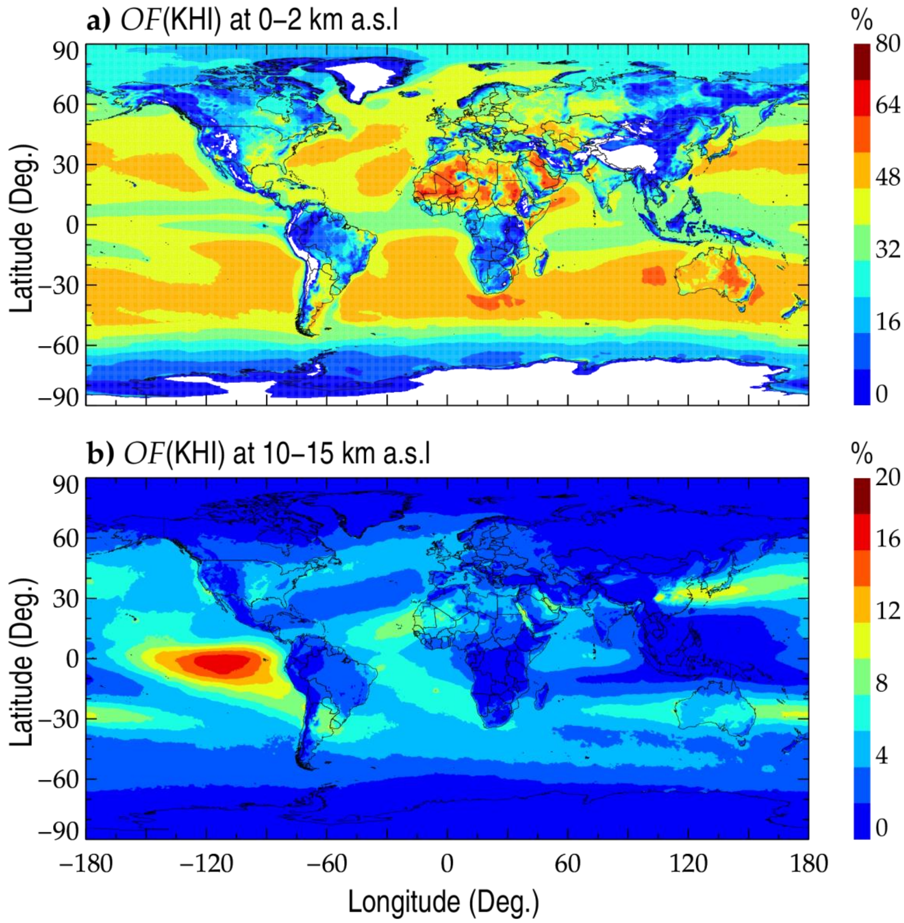

Figure 8. The spatial distribution of the mean occurrence frequency of KHI in ERA5 reanalysis at 0–2 km a.s.l (a) and 10–15 km a.s.l (b). Note that the threshold value of *Ri* is set to 1.

https://doi.org/10.5194/acp-2022-851
Preprint. Discussion started: 20 February 2023

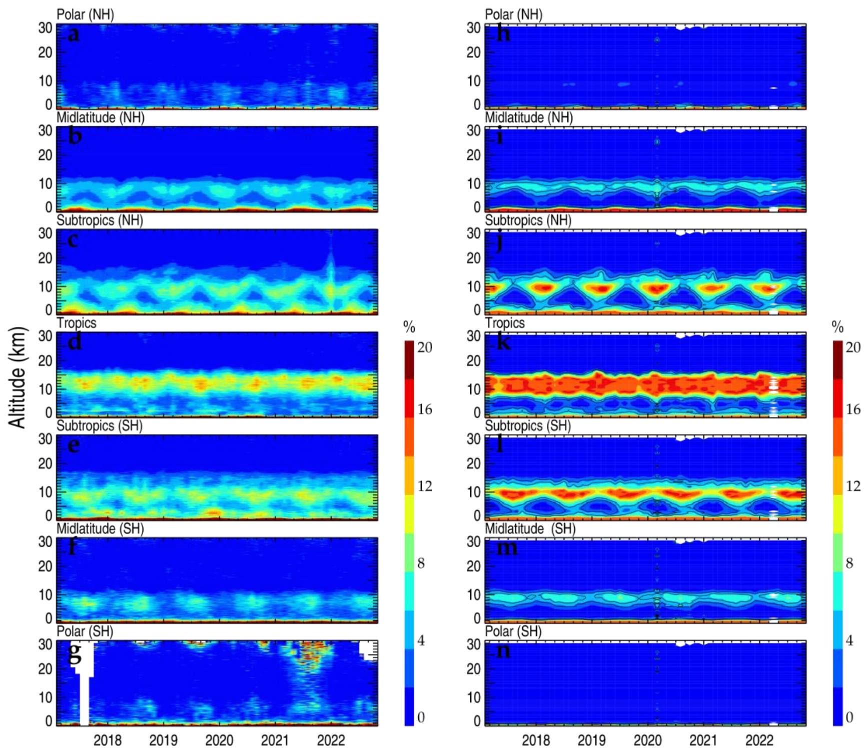

Figure 9. The monthly averaged *OF*(KHI) in the HVRRS (a–g) and ERA5 reanalysis (h–n) in seven climate zones. NH=Northern Hemisphere; SH=Southern Hemisphere.

https://doi.org/10.5194/acp-2022-851
Preprint. Discussion started: 20 February 2023

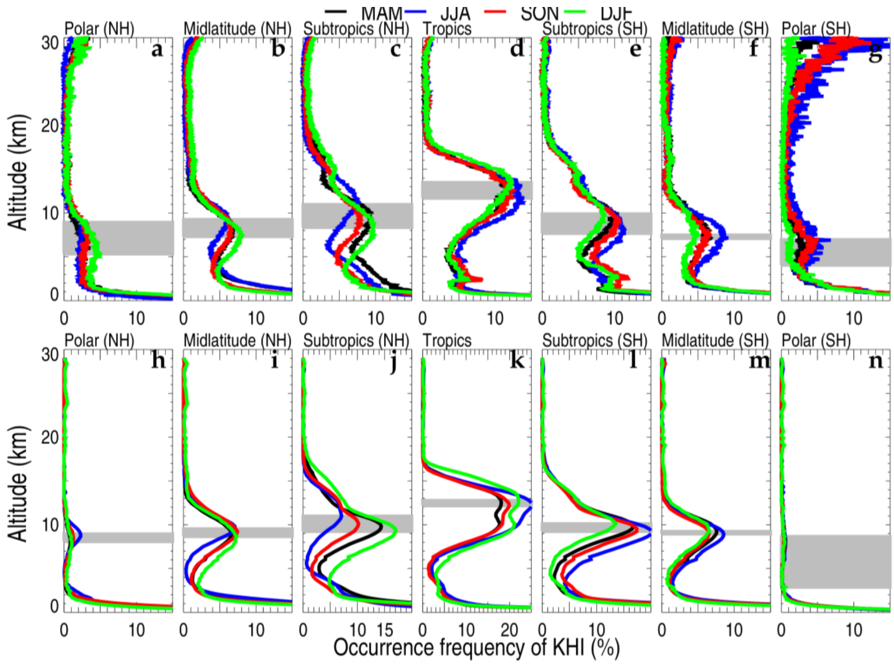

Figure 10. The seasonal averaged *OF*(KHI) in the HVRRS (a–g) and ERA5 reanalysis (h–m) in seven climate zones. The gray areas indicate the free tropospheric regime with maximal *OF*(KHI) in four seasons. MAM, March–April–May; JJA, June–July–August; SON, September–October–November; DJF, December–January–February. NH=Northern Hemisphere; SH=Southern Hemisphere.

https://doi.org/10.5194/acp-2022-851
Preprint. Discussion started: 20 February 2023

Atmospheric Chemistry and Physics Discussions
Open Access
EGU

781

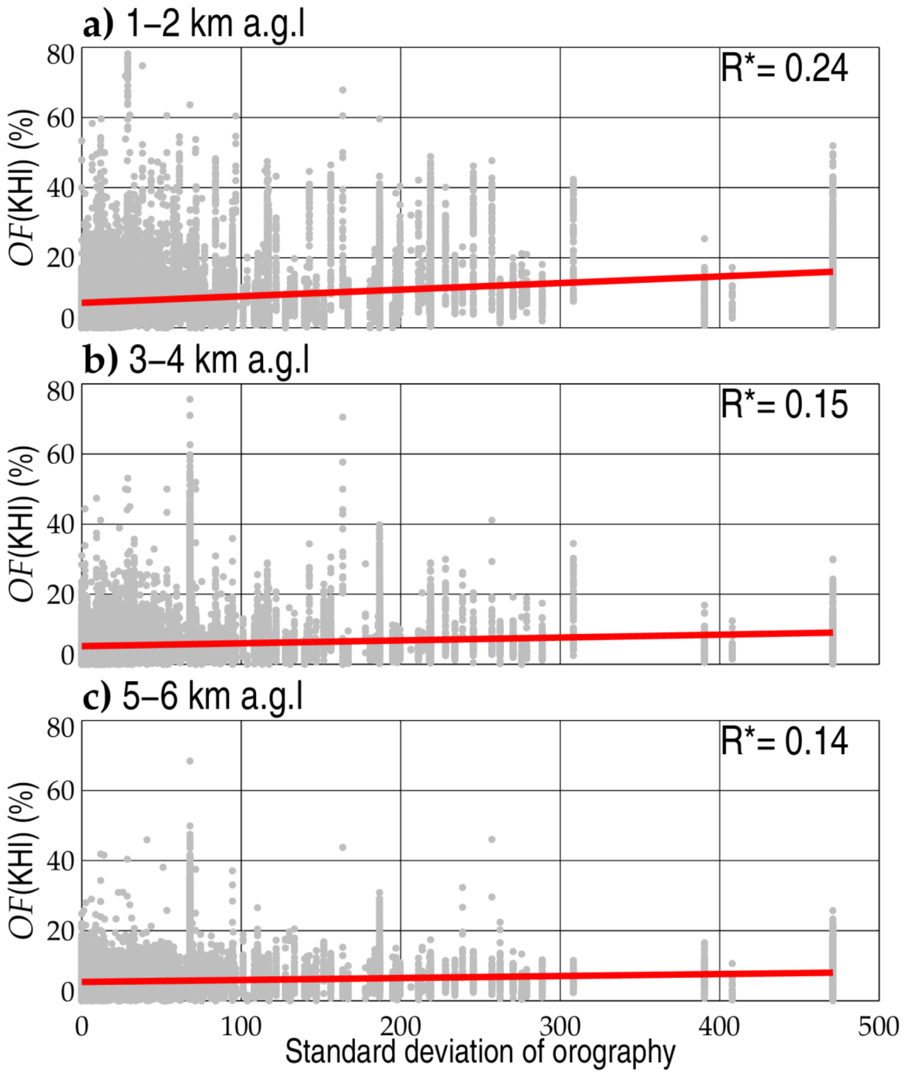

782

783 **Figure 11**. The association of HVRRS-determined *OF*(KHI) with different standard
784 deviations of orography. (a), (b), and (c) are for height ranges of 1–2 km, 3–4 km, and
785 5–6 km a.g.l, respectively. The correlation coefficients between *OF*(KHI) and
786 standard derivation of orography are marked in the top right corner, where the star
787 superscripts indicate that values are statistically significant ($p<0.05$).

788

https://doi.org/10.5194/acp-2022-851
Preprint. Discussion started: 20 February 2023

Atmospheric Chemistry and Physics
Discussions

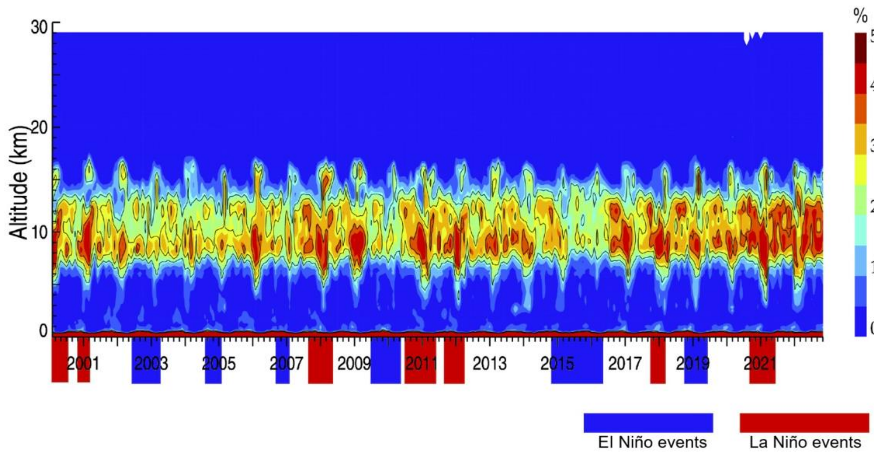

Figure 12. The monthly averaged *OF*(KHI) in ERA5 reanalysis over the Niño 3 region (5 ° N–5 ° S, 150 ° W–90 ° W). The blue and red shadings in time axis indicate the time periods with EI Niño and La Niño events, respectively.

https://doi.org/10.5194/acp-2022-851
Preprint. Discussion started: 20 February 2023

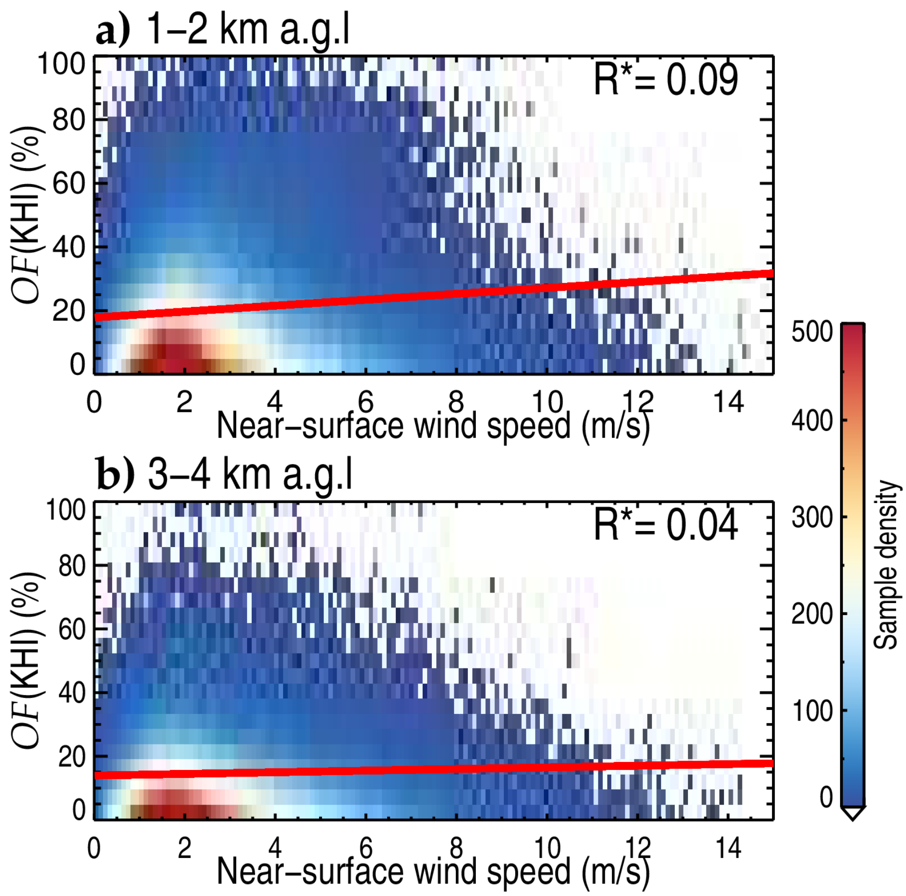

Figure 13. Density plots of HVRRS-derived *OF*(KHI) over terrain with standard deviation of orography larger than 50 as a function of near-surface wind speed. The red lines represent a least-squared linear regression. The star superscripts indicate that values are statistically significant ($p<0.05$).

https://doi.org/10.5194/acp-2022-851
Preprint. Discussion started: 20 February 2023

Atmospheric Chemistry and Physics
Open Access
Discussions

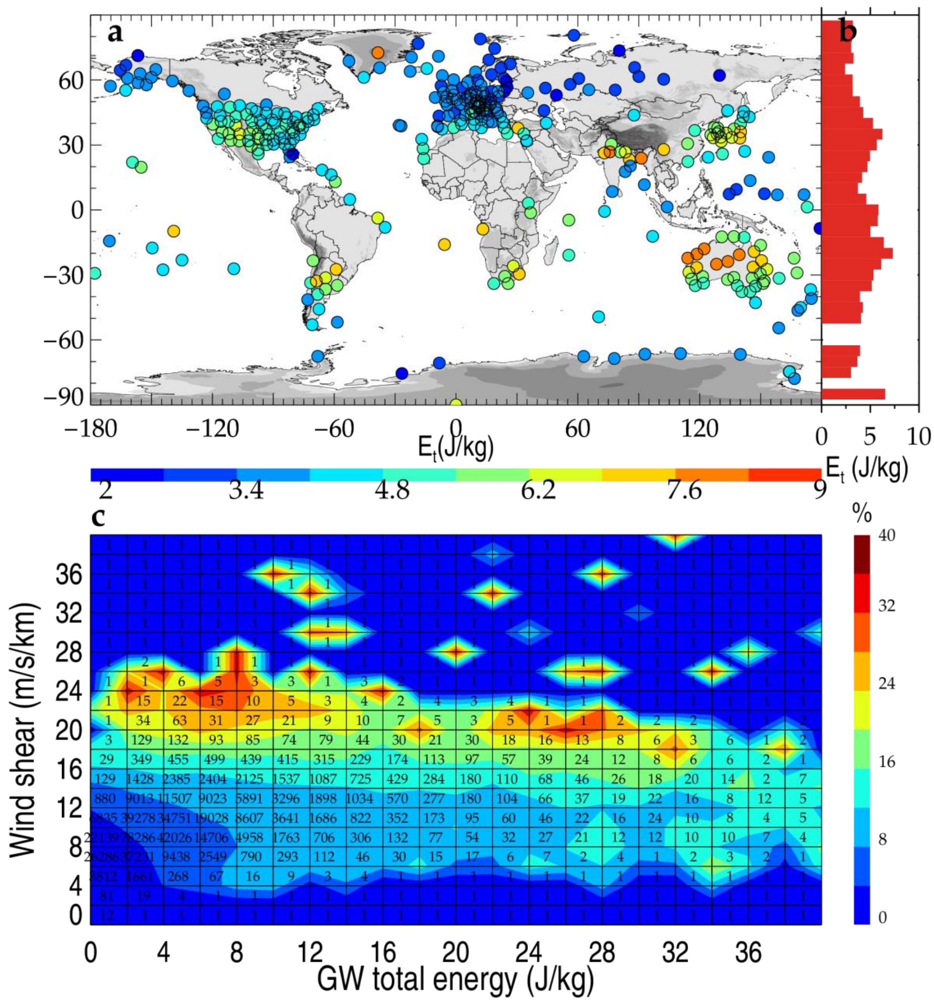

Figure 14. Geographical distribution of mean tropospheric GW total energy obtained from the HVRRS (a). The latitudinal variation of mean energy in a grid cell of 5° latitude (b). The joint distribution of *OF*(KHI) with GW energy and wind shear (c). The *OF*(KHI) and wind shear are derived from individual HVRRS profiles and vertically averaged over the tropospheric segment that is used for GW study. The numerical number in (c) indicates the matched profile number in each grid, using a bin size of 2 J/kg along the x axis and 2 m/s/km along the y axis.

https://doi.org/10.5194/acp-2022-851
Preprint. Discussion started: 20 February 2023

Atmospheric Chemistry and Physics
Open Access
EGU
Discussions

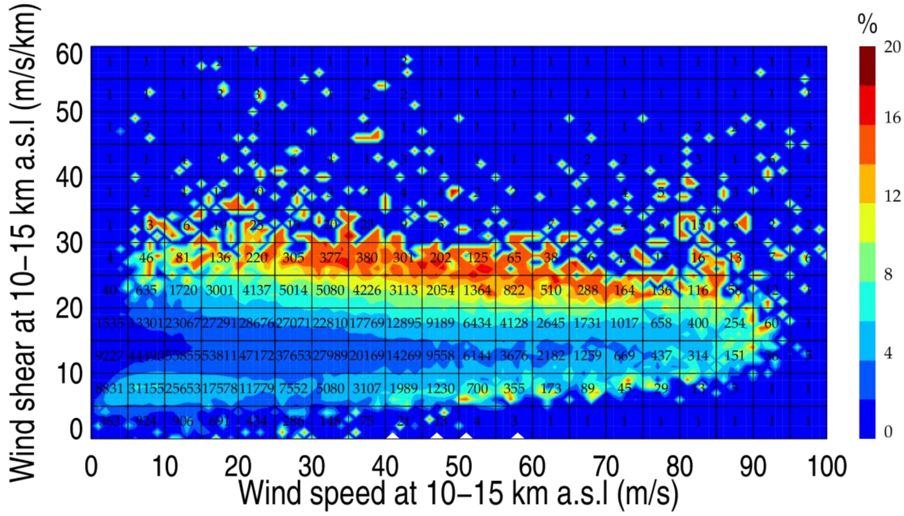

Figure 15. Joint distribution of HVRRS-derived wind speed, wind shear, and *OF*(KHI), with a bin size of 5 m/s along the x axis and 5 m/s/km along the y axis. Note that all the relationship is based on the mean result of individual profiles at heights of 10–15 km a.g.l. The number indicates the matched profile number in each grid.